A Multisensor Comparison of Experimental Oil Spills in Polarimetric SAR for High Wind Conditions

Stine Skrunes, *Member, IEEE,* Camilla Brekke, *Member, IEEE,* Cathleen E. Jones, *Member, IEEE,* and Benjamin Holt, *Member, IEEE*

***Abstract*—In this paper we present the experimental setup and data collection during the *NOrwegian Radar oil Spill Experiment 2015 (NORSE2015)*, followed by a comparison of a subset of the multisensory SAR imagery collected during the experiment. Multipolarization synthetic aperture radar (SAR) data acquired by Radarsat-2, TerraSAR-X and the Uninhabited Aerial Vehicle Synthetic Aperture Radar (UAVSAR) less than six minutes apart are investigated and compared. All three sensors detect the four slicks of varying physiochemical composition under challenging conditions posed by small slicks in high wind conditions of $\sim$12 m/s. The detectability is best in TerraSAR-X and UAVSAR. The high wind allows for large signal-to-noise ratios over the slicks, even in the satellite data and in cross-polarization channels. Although detection is possible, discrimination between slick types, using multipolarization parameters previously found useful for this purpose, is not possible under these conditions for the acquisitions in the instance studied.**

***Index Terms*—oil slick, characterization, detection, multi-frequency, multi-polarization features, sensor comparison, synthetic aperture radar, high wind**

I. Introduction

Synthetic aperture radar (SAR) is a well established tool for operational monitoring of vast ocean areas in order to detect marine oil spills, both accidental releases and illegal discharges from ships [1]. These sensors can also be used as part of oil spill response and clean up operations after large scale accidents such as the Deepwater Horizon in the Gulf of Mexico in 2010 [2]. However, some unanswered questions still remain for the use of SAR in oil spill observation, including how to discriminate between oil spills and look-alikes (i.e., natural phenomena that produce similar SAR signatures as oil films), and how to extract more information about a detected spill, in particular slick thickness, volume and relative oil content. These questions are frequently addressed in the literature using SAR polarimetry and multipolarization features (see, e.g., [3]–[8]). Most of these studies are based on data obtained under low-medium winds, and more information on potential oil spill detection and characterization at higher winds is needed. Sensor properties such as frequency, polarization, observation geometry, resolution and noise floor also affect the SAR measurements and hence the oil spill detection and characterization capabilities. In oil spill remote sensing, there is a need for frequent data acquisitions over large ocean areas, hence the full set of available SAR sensors suitable for this application should be used in combination. During a response operation, airborne SAR sensors that can provide rapid repeat acquisitions are valuable for closely following a slicks evolution and drift. Mapping the detection and characterization capabilities of various sensors, as well as the conditions under which they can be used, is important for improving the overall knowledge and applicability of SAR for oil spill remote sensing.

In the literature, only a few studies comparing the oil spill signatures measured by different sensors and/or frequency bands in multipolarization mode can be found. The most well-known study is [9], where multifrequency (C-, X- and L-band) data from the Spaceborne Imaging Radar-C/X-Band Synthetic Aperture Radar (SIR-C/X-SAR) were investigated. In [10], the detection and characterization capabilities of multipolarization SAR data from three pairs of near-coincident Radarsat-2 and TerraSAR-X scenes were compared. Some differences were observed between the sensors in terms of scattering type, statistical characteristics and the characterization ability using multipolarization features. However, the need for further investigations, particularly of data at more comparable incidence angles and for varying slick types and weather conditions, was noted. Obtaining real SAR data from the operational surveillance sensors to investigate these issues can be challenging, as oil spill events are not known beforehand and ground truth information may not be available.

In this paper, we present and analyze data from a controlled oil spill experiment, the *NOrwegian Radar oil Spill Experiment 2015 (NORSE2015)*, that took place in the North Sea in June 2015. NORSE2015 was a joint experiment between UiT The Arctic University of Norway (UiT) and the Jet Propulsion Laboratory (JPL) / National Aeronautics and Space Administration (NASA) done in collaboration with the Norwegian Clean Seas Association for Operating Companies (NOFO). The experiment was designed for systematic collection of X-, C- and L-band SAR data over surface slicks with varying, known properties. In this paper, we investigate three of the scenes collected during NORSE2015, acquired with different SAR sensors operating at different frequencies,

This study is funded through the RCN projects GlobOilRisk (BIA, project no.: 235444/O30) and CIRFA (RCN grant no. 237906).

S. Skrunes and C. Brekke are with the Department of Physics and Technology, University of Tromsø - The Arctic University of Norway, 9037 Tromsø, Norway (e-mail: stine.skrunes@uit.no, camilla.brekke@uit.no).

C. E. Jones and B. Holt are with the Jet Propulsion Laboratory, California Institute of Technology, Pasadena, CA, USA, (e-mail: cathleen.e.jones@jpl.nasa.gov, benjamin.m.holt@jpl.nasa.gov).

Manuscript received ; revised .

all in multipolarization mode. The three scenes are acquired within a time period of only six minutes and under high wind conditions ($\sim$12 m/s). The current study is building onto the work presented in [10], by including a third sensor, using data at more comparable incidence angles, with four different slick types present in all scenes, and acquired in a higher wind speed regime than the previous study.

The analysis is conducted on near-coincident multipolarization Radarsat-2 (RS2) C-band, TerraSAR-X (TSX) X-band and Uninhabited Aerial Vehicle Synthetic Aperture Radar (UAVSAR) L-band data, each containing the same four slicks of varying properties. The main objectives of this paper are i) to present the experimental setup and data collection of NORSE2015, ii) to investigate and compare the multipolarization SAR signatures of the experimental slicks as measured by RS2, TSX and UAVSAR, and iii) compare the results here obtained under high wind conditions to previous analyses for low wind data. The data are analysed in terms of slick detectability, noise levels, and multipolarization features related to, e.g., scattering properties and statistical characteristics.

The paper is organized as follows: Section II provides the background for the study. The experimental setup and data collection of NORSE2015 are presented in Section III, and the results of the multisensor analysis are given in Section IV. Conclusions drawn from the study are presented in Section V.

II. SAR REMOTE SENSING OF OIL

Oil spills are detected as areas of reduced backscatter, mainly due to a reduction in the small scale surface roughness caused by the oil film [11]. A reduction in the effective dielectric constant can also lead to a decrease in the backscatter energy if the oil spill is sufficiently thick, or if oil is mixed into the water in high enough concentrations in a layer below the surface [3], [12]. The SAR imaging of oil spills depends on both slick characteristics, environmental conditions and sensor properties. The following subsections address some of these factors, providing a background for the following analysis.

A. Sensor parameters

A number of sensor parameters can affect the SAR imaging and the potential for oil slick detection and characterization, including incidence angle, polarization, frequency and noise floor.

In general, the ocean backscatter decreases as the incidence angle θ increases [13], and the most useful angles for observing oil spills are 20° to 45° [14]. For moderate incidence angles, the slick-sea contrast have been found to increase with θ in, e.g., [3], [15]. At higher θ, the signal-to-noise ratio (SNR), i.e., the ratio between backscatter level and the sensor noise equivalent sigma zero (NESZ), is reduced, limiting the use of these data for oil spill observation [3], [4], [10], [16]. The HH polarization channel (horizontal transmit and horizontal receive) decreases faster than the VV polarization channel with increasing incidence angle, i.e., from near range to far range, and hence approaches the noise floor more quickly. VV is considered the preferred channel for oil spill detection. The cross-polarization channels (HV and VH) lie much lower than the copolarization channels and are generally regarded as less useful for detecting oil slicks. Over the last decade, research has been increasingly focusing on the potential of using multipolarization data, i.e., a combination of two or more polarimetric channels, for the task of oil slick *characterization*. This includes the discrimination of oil spills from look-alikes and the extraction of more slick information, e.g., relative thickness variations and oil-water ratio. Most of the work have utilized the linear polarization transmit and receive channels from the scattering matrix

$$\mathbf{S} = \begin{bmatrix} S_{HH} & S_{VH} \\ S_{HV} & S_{VV} \end{bmatrix} = \begin{bmatrix} |S_{HH}|e^{j\phi_{HH}} & |S_{VH}|e^{j\phi_{VH}} \\ |S_{HV}|e^{j\phi_{HV}} & |S_{VV}|e^{j\phi_{VV}} \end{bmatrix}, \quad (1)$$

where $|S_{xx}|$ and ϕ_{xx} denote the amplitudes and the phases of the measured complex scattering coefficients. More recently, compact polarimetry, e.g., using circular transmit and linear receive polarizations, has also been applied for this purpose. A recent review on oil spill observation using multipolarization techniques, including compact polarimetry, can be found in [6]. When the aim is oil slick characterization, and particularly when cross-polarization data are included, it is important to take into account the noise floor and resulting SNR. Low SNR may affect multipolarization parameters and lead to misinterpretation of results [3].

Sensors operating in the C-band (3.75-7.5 GHz) frequency range have traditionally been regarded as the most suitable for oil spill observation, but historically has also been the most widely flown SAR frequency. Currently, both X-band (7.5-12 GHz) and L-band (1-2 GHz) sensors are increasingly available and used for this application. The radar frequency determines the surface roughness scale observed by the radar and the penetration depth of the signal into the medium. As ocean backscatter is dominated by the return from surface roughness on the same scale as the radar wavelength, L-band sensors observe longer surface waves compared to C- and X-band sensors [13]. The penetration depth is typically a few mm-cm for clean sea surface, and increases with wavelength. Hence, L-band SAR will see further into the water column than C- and X-band sensors [17]. Whether changes in the dielectric properties of the surface due to the presence of a surface film can be detected by a SAR sensor depends on the thickness of the oil layer. This again depends on the properties of the substance and weathering mechanisms acting on the film (see, e.g., [10] for further discussions).

The theoretical signal dampening of oil as function of wavelength was shown in [18] to increase with frequency at fixed wind speed and incidence angle. Some empirical [9], [16], [19], [20] and simulation [15] studies in the literature support this. However, some studies have also found results in contradiction to this observation [21]. A discussion of the effect of different marine surface films on the wave properties and thereby on the radar contrast was given in [9]. Multifrequency data were found capable of discriminating between different types of surface films under low to moderate wind speeds. A difference in the damping behavior between biogenic slicks and mineral oil films was observed, particularly at L-band, where biogenic films showed larger damping characteristics [9].

As true multifrequency data are generally not available, near-coincident data from various sensors are applied to compare the oil spill detection and characterization capabilities of different frequency bands. Only a few studies on this topic using multipolarization data can be found, e.g., [10], [16]. In [10], three pairs of near-coincident RS2 and TSX acquisitions were compared. No clear sensor preference was identified in terms of damping ratios and SNR. However, multipolarization features showed better between-region discrimination in RS2 than in TSX. Differences in scattering characteristics and statistical properties were also observed, with a larger contribution of non-Bragg scattering and a larger deviation from Gaussian statistics in the TSX data. However, it was noted that the difference in incidence angle between the RS2 and TSX scenes could affect the results.

The current paper aims to build on the findings of [10], comparing three different sensors and further addressing the effects of varying sensor properties and weather conditions.

B. Environmental conditions

When the wind speed increases, the sea surface roughens, resulting in higher SAR backscatter [13]. The shorter surface waves are the first to be generated (decay) as the wind speed grows (falls). Hence, changes in wind speed are more quickly reflected in the backscatter of higher frequency radars [22]. Although the ocean backscatter is dominated by returns from the small surface waves on the scale of the radar wavelength, it is modified by the longer waves on which they travel. This apparent modulation of the Bragg waves by the longer waves allows for the latter to be visible in SAR images. These mechanisms include the tilt modulation, hydrodynamic modulation and velocity bunching. The first two are most sensitive to wave components in the range direction, whereas the latter allows for SAR to image ocean waves with an azimuth-traveling component, using the Doppler shift and the orbital motion of the ocean surface [23]. However, a SAR sensor can only sense wave components larger than the so-called azimuth cut-off wavelength, which can be estimated as

$$\Lambda_{\min} = \frac{R}{V}\sqrt{H_s}. \tag{2}$$

The cut-off grows with the range (R)-to-velocity (V) ratio of the SAR platform, and with the significant wave height (H_s) [23].

Oil spills can only be detected within a limited range of wind speeds. Too low wind does not allow for a sufficient contrast in surface roughness between slicks and clean sea. On the other hand, at very high winds, the damping effect of the oil can be counterbalanced and the turbulence may stir and mix and/or sink the oil. Oil spill detection is considered possible in wind speeds from approximately 1.5 to 15 m/s, with ideal conditions at about 3-10 m/s [24], [25].

The damping behavior of oil slicks has been found to be strongly dependent on wind conditions. Both measured and simulated oil slick damping ratios have been reported to decrease with increasing wind speed [9], [15], [16], [26]. In [9], the potential for slick characterization using multifrequency data was severely reduced at high wind speed (12 m/s) as only slight differences were measured in the damping behavior of different substances under these conditions.

In this paper, oil slicks are imaged under high wind conditions. Hence, the capabilities of multipolarization SAR for oil slick detection and characterization in high wind can be investigated, and compared to similar analyses done in the past for low wind situations.

III. Experimental setup and data collection

NORSE2015 took place 10 June 2015, at the abandoned Frigg field in the North Sea around 59°59′ N, 2°27′ E. It was a collaboration between UiT, JPL/NASA and NOFO and was carried out during NOFO's annual oil-on-water exercise. The experimental setup and data collection are described in the following sections.

A. Experimental setup

The objective of NORSE2015 was to collect X-, C- and L-band SAR data over surface slicks with varying, known properties. Four substances were released close in time and imaged from several airborne and satellite borne remote sensing platforms. Specifically, three emulsions with the same composition but with varying oil volumetric fraction, i.e., 40% (E40), 60% (E60) and 80% (E80), were released, in addition to one release of plant oil (P) for simulation of a natural biogenic slick (see [4]). The four substances were released along a line approximately parallel to the flight (azimuth) direction of the SAR sensors in order for the incidence angle of all releases to be the same in each radar image. The releases were lined up towards the middle of the scenes to maximize the SNR. It took about 47 minutes to do the four discharges, which were done with a spatial separation of about 0.5 nautical miles between release points. The plant oil was released first followed by the emulsions with increasing oil content to preserve the relative oil volume fraction between the slicks over time. The releases were timed so that the slicks would have at least about one hour to spread out before the morning satellite overpasses. The emulsions were produced by NOFO and consisted of a mix of Troll crude oil, Oseberg crude oil and One-Mul emulsifier. All four releases were left untouched on the surface. More details on the releases are provided in Table I, and a photo is shown in Fig. 1(a).

During the experiment, SAR data were collected by various sensors from both airborne and spaceborne platforms. In addition, meteorological and oceanographic (metocean) data were collected from ships, radiosondes, drifters and buoys. Optical imagery was also acquired from the ships. The collected data are further described in the next sections.

B. SAR data set

During the day of NORSE2015, the four releases described in Table I were imaged from several spaceborne SAR sensors, as well as from the NASA UAVSAR. The latter had two flights, each lasting several hours, acquiring a time series of the evolving slicks consisting of 22 scenes. Table II gives an overview of the SAR data acquired over the experiment on the

TABLE I: Properties of the experimental oil releases.

Release	Time (UTC)	Substance	Volume
P	04.48	Plant oil: Radiagreen ebo	0.2 m^3
E40	04.59	Emulsion (40% oil): 300 L water + 100 L Troll + 100 L Oseberg + 0.2 L One-Mul	0.5 m^3
E60	05.15	Emulsion (60% oil): 200 L water + 150 L Troll + 150 L Oseberg + 0.2 L One-Mul	0.5 m^3
E80	05.30	Emulsion (80% oil): 100 L water + 200 L Troll + 200 L Oseberg + 0.2 L One-Mul	0.5 m^3

(a)

(b)

Fig. 1: Photos taken from the release vessel, (a) E80 right after release, (b) sea state at 07.42 UTC. Photos by Øyvind Breivik.

TABLE II: SAR data set acquired during NORSE2015. SM: stripmap, WFQ: wide fine quad, FRS: fine resolution stripmap, HS: high-sensitive, freq.: frequency, pol.: polarization.

Sensor	Time (UTC)	Mode	Freq. band	Polarization
UAVSAR (16 scenes)	05.32-08.53	PolSAR	L-band	Quad-pol.
TSX	06.24	SM	X-band	Dual-pol. (HH, VV)
RS2	06.28	WFQ	C-band	Quad-pol.
RISAT-1	07.19	FRS	C-band	Compact pol. (RH, RV)
UAVSAR (6 scenes)	11.45-13.18	PolSAR	L-band	Quad-pol.
TSX	17.12	SM	X-band	Dual-pol. (HH, VV)
ALOS-2	23.53	HS	L-band	Single-pol. (VV)

10 June. This is a unique data set that allows for a variety of investigations on SAR remote sensing of oil. A comparison of quad-polarization RS2 and compact polarization Radar Imaging Satellite 1 (RISAT-1) data was presented in [27].

In the current paper we investigate three of the SAR scenes acquired by RS2, TSX and UAVSAR. The RS2 and TSX scenes are the morning passes on 10 June, which were used as a baseline when timing the releases. For comparison, we investigate the UAVSAR scene acquired closest in time to the satellite overpasses. More information about these three scenes are provided in Table III. Fig. 2 shows a map of the experiment area, scene coverages and release positions.

C. Metocean data

Meteorological and oceanographic information were collected onboard the release vessel, as well as from weather balloons, drifters and buoys. The balloons were released at different times throughout the day, whereas the drifters and buoys were set out together with the oils. These included two iSphere drifters, which are designed to drift with the oil slicks (experiences windage) [31] and two Iridium Self Locating Datum Marker Buoys (iSLDMB), which are completely submerged (no windage, experiences near surface current drift) [32]. A comparison of modeled oil drift from both types of drift buoys with the actual drift obtained from the UAVSAR time series will be presented in a separate paper.

Metocean data from the 24 hours prior to SAR acquisitions are presented in Table IV and a photo of the sea surface taken about 80 minutes after the SAR acquisitions is included

TABLE III: Properties of the three scenes used in the sensor comparison [28]–[30]. Numbers given in parentheses are the relevant values at the slick positions. Rg: range, az: azimuth, asc.: ascending, desc.: descending, R: right, L: left.

Sensor	Time (UTC)	Mode (beam)	Freq. [GHz]	Polarization	Incidence angle	NESZ [dB]	Resolution[a] (rg × az) [m]	Scene size[a] (rg × az) [km]	Pass/look direction (heading)
TSX	06.24	SM (StripNear_006)	X-band (9.65)	Dual-pol. (HH, VV)	27.3° - 29.0°	-26.4 - -23.7	1.2 × 6.6	15 × 50	Desc./R (193°)
RS2	06.28	WFQ (FQ5W)	C-band (5.405)	Quad-pol.	22.6° - 26.0° (24°)	-37.2 - -26.2	5.2 × 7.6	50 × 25	Desc./R (197°)
UAVSAR	06.26 -06.30	PolSAR	L-band (1.26)	Quad-pol.	19.5° - 67.5° (46° - 48°)	∼ -48 - -33 (∼ -47)	2.5 × 0.9	20 km swath	Asc./L (7°)

[a] Values are not scene specific but general values for the relevant sensor and mode.

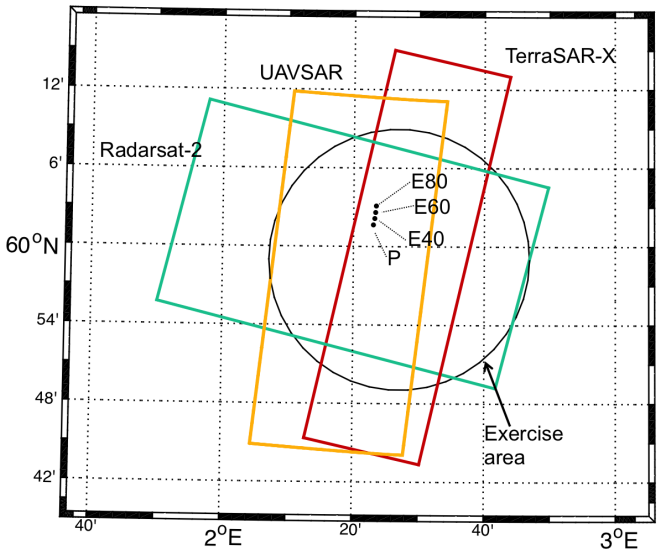

Fig. 2: Map of the exercise area, scene coverages and release positions.

in Fig. 1(b). As can be seen from Table IV, the weather conditions were quite rough during the experiment. At the time of the four oil releases, the discharging ship measured wind speeds of 9-11 m/s from a SW-W direction, a wave height of 2.5 m and a temperature of 9°C. At 06.18 UTC, which is the weather observation closest in time to the SAR overpasses, a wind speed of 12 m/s from a direction of 260° was logged. This is in the upper part of the wind speed range where oil spill detection is considered possible (see Section II-B). It should be noted that the H_s in Table IV is estimated visually and is therefore a rough measure.

In addition to the in situ measurements, information on wind and wave conditions is retrieved from the RS2 and TSX data [33], [34] and presented in Table V (similar analysis of the UAVSAR data is not performed as a suitable method is not currently available). The information is obtained from an area close to, but not covering, the slicks. It can be seen from Table V that the various estimates of wave and wind conditions are quite similar. The estimated wind speeds are a little lower than the closest in situ observations. It can be noted that the SAR derived wave direction does not match the in situ observed wind direction. Hence, the wave system observed in the SAR spectra may not be the local wind, but rather a second wave system originating further out at sea. The local wind sea may be more difficult to detect in the SAR spectra due to azimuth cutoff effects. The azimuth cut-off given in Table V is retrieved from the wave spectra (see [34]) for RS2 and TSX, and estimated using (2) for UAVSAR. The former method is more accurate than the latter. The cut-off wavelengths are quite high, particularly for the satellite sensors. This indicates that the imaging process may be non-linear, which could reduce the ability of the SAR to accurately sense the azimuth wave component.

The environmental conditions during NORSE2015 are very different from those during previous oil-on-water exercises (see, e.g., [4], [10]), which allows an interesting comparison of detection and characterization potential in terms of weather conditions.

TABLE IV: Metocean data from 9 and 10 June 2015. The two days are separated by the horizontal line.

Time (UTC)	Measured from	Wind speed [m/s] (direction)	H_s [m]	Temperature air (sea surface)
06.20	Ship	5 (246°)		
08.20	Ship	5 (268°)		
09.30	Ship	5 (254°)		
11.50	Ship	7 (247°)		
12.08	Ship	8 (247°)		
13.03	Ship	7 (253°)		
15.03	Ship	7 (254°)		
18.47	Ship	9 (250°)		
04.30	Ship	12	2.5	10°C
04.50	Ship	11	2.5	9°C
05.34	Ship	9 (248°)		
06.18	Ship	12 (260°)		
06.52	Balloon			10.2°C
05.00 - 23.50	Drifters			(9.9°C - 10.2°C)

IV. Multisensor analysis

In the following sections, we compare the three near-coincident scenes described in Table III in terms of data quality and polarimetric content. As the scenes are collected very close in time, we assume that slick properties and environmental conditions are constant between the acquisitions. Hence, any differences observed between the scenes should be related only to sensor parameters such as frequency, resolution, incidence angle and noise floor. The results are also compared to previous findings, which primarily evaluated data acquired under lower wind conditions.

TABLE V: Wind and wave information retrieved from the SAR data for RS2 and TSX [33], [34]. $\hat{H}_s$ denotes the significant wave height estimated from the wave spectra. Wave direction is the direction the waves are travelling towards. Azimuth cut-off is retrieved from the data for RS2 and TSX (see [34]) and estimated using (2) for UAVSAR.

	Wavelength	Wave direction	$\hat{H}_s$	Azimuth cut-off	Wind speed
TSX (VV)	172 m	129°	2.3 m	210 m	10.9 m/s
TSX (HH)	172 m	129°	2.4 m	209 m	10.8 m/s
RS2 (VV)	171 m	128°	2.2 m	279 m	10.0 m/s
RS2 (HH)	172 m	128°	2.3 m	271 m	10.7 m/s
UAVSAR				107 m	

A. Detectability

Intensity images of the relevant subscenes are shown in Fig. 3, with the slick identities and areas indicated in the UAVSAR scene. The images are in radar coordinates. The oil slicks are seen as areas of reduced backscatter compared to the surrounding clean sea. In situ measurements of slick thickness were not possible during the experiment. However, using the information on release volumes and areas retrieved from the UAVSAR data (see, Fig. 3(c)), the thicknesses can be estimated. Following this approach, the average slick layer thicknesses are found to be in the range 1.3 - 1.7 μm for the emulsions and 0.7 μm for the plant oil. These thicknesses are much lower than the expected penetration depth (see Section II), and hence, the change in dielectric constant due to the presence of the oil may not contribute much to the reduction in backscatter, for any of the sensors. However, weathering mechanisms that could alter the thicknesses are not accounted in these estimates.

Fig. 3 shows that all four releases are visible in each scene (in both VV and VH), but the slicks are less clearly distinguished in the RS2 scene compared to TSX and UAVSAR. The coarser resolution of RS2 (see Table III) could, at least in part, cause the degraded contrast in this case. The releases are quite small in volume and areal extent, and the larger pixel size of RS2 can lead to more mixed sea/slick pixels, and hence reduce the overall class separation. The best visual slick-sea contrast is observed in the UAVSAR data. The higher incidence angle in this scene (46° - 48° compared to $\sim$24° and $\sim$28° in RS2 and TSX, respectively) may contribute to the enhanced contrast in this case. The E60 slick has the best visual slick-sea contrast, which may be due to the higher oil volume content than E40 and a longer time on the surface than the E80. A separate study on the temporal changes in slick-sea contrasts as the slicks evolve is on-going based on the full UAVSAR time series described in Table II.

A strong wave pattern can be clearly seen over the images in Fig. 3. The pattern is particularly pronounced in the satellite scenes, making it more difficult to identify the slick boundaries. This is probably the wave system described in Table V. Note that the wave pattern is less pronounced in the cross-polarization channel compared to the copolarization channel, particularly for RS2. The azimuth cut-offs estimated from the data are quite high (see Table V) due to the high sea state. The largest cut-off is found in RS2 (270-280 m) and the lowest in UAVSAR (107 m). This factor may also contribute to the degraded slick-sea contrast in the RS2 case. Hence, a combination of different sensor-related parameters including resolution, incidence angle and azimuth cut-off contributes to the relative differences in detectability among the sensors.

The RS2 and TSX scenes have also been analyzed at Kongsberg Satellite Services (KSAT) in Tromsø, Norway, as part of their operational oil spill detection service. Their analysis reports for these two scenes also show a difference in the slicks detectability between the sensors. In the TSX case, all four releases were detected and assigned to detection category A, i.e., high confidence detection. In RS2 however, only three of the regions were detected and labeled as category B, i.e., low confidence detection. The E80 slick was not detected using their algorithm. These findings indicate that under these conditions, i.e., for small slicks and rough seas, and under relatively low incidence angles, the limit of what can be detected with RS2 is being approached.

Intensity variations along lines traversing the slicks are shown in Fig. 4. The lines are selected along the longest axes of the slicks, i.e., not entirely aligned with the range direction, and contain some clean sea pixels on each side of the slick. The profiles are obtained by averaging the intensity over 20 pixels in the azimuth direction, and then over 20 pixels along the line, using a sliding window. The approximate positions of the edges of the slicks are indicated by the vertical dashed lines. A reduction in the backscatter values over the slicks is observed in all cases. The reduction is generally larger in TSX and UAVSAR than in RS2, as expected from Fig. 3. The difference in damping between the slick types is very small for all sensors. This may be related to the high wind during the overpasses, reducing the contrast in surface roughness between slicks and sea, impeding the differences between slicks. This is consistent with the findings in [9] (see Section II-B).

In the following subsections, manually segmented regions of interest (ROIs) are used to investigate the slick characteristics. It should be noted that the wave patterns over the images can reduce the accuracy of the segmentation, particularly in the case of RS2, and is a source of uncertainty.

B. Noise analysis

When the aim is slick characterization, in addition to just detection, the sensor noise floor is an important factor to consider. Because oil spills are low backscatter regions, the backscattered signal can approach, and fall below, the sensor noise floor, NESZ. This is a problem especially in the cross-polarization channels. In [4], [10], [16], noise analyses of RS2 quad-polarization data and TSX dual-copolarization data (i.e., HH and VV) were presented. It was found that a large part of the cross-polarization signal lay below the noise floor, and it was suggested to use only the HH and VV channels, which had much better SNRs. One major advantage of the UAVSAR is the very low NESZ of about -48 dB at its minimum [28]. This sensor can therefore be very useful for observing and characterizing low backscatter phenomena such as oil spills (see, e.g., [3]).

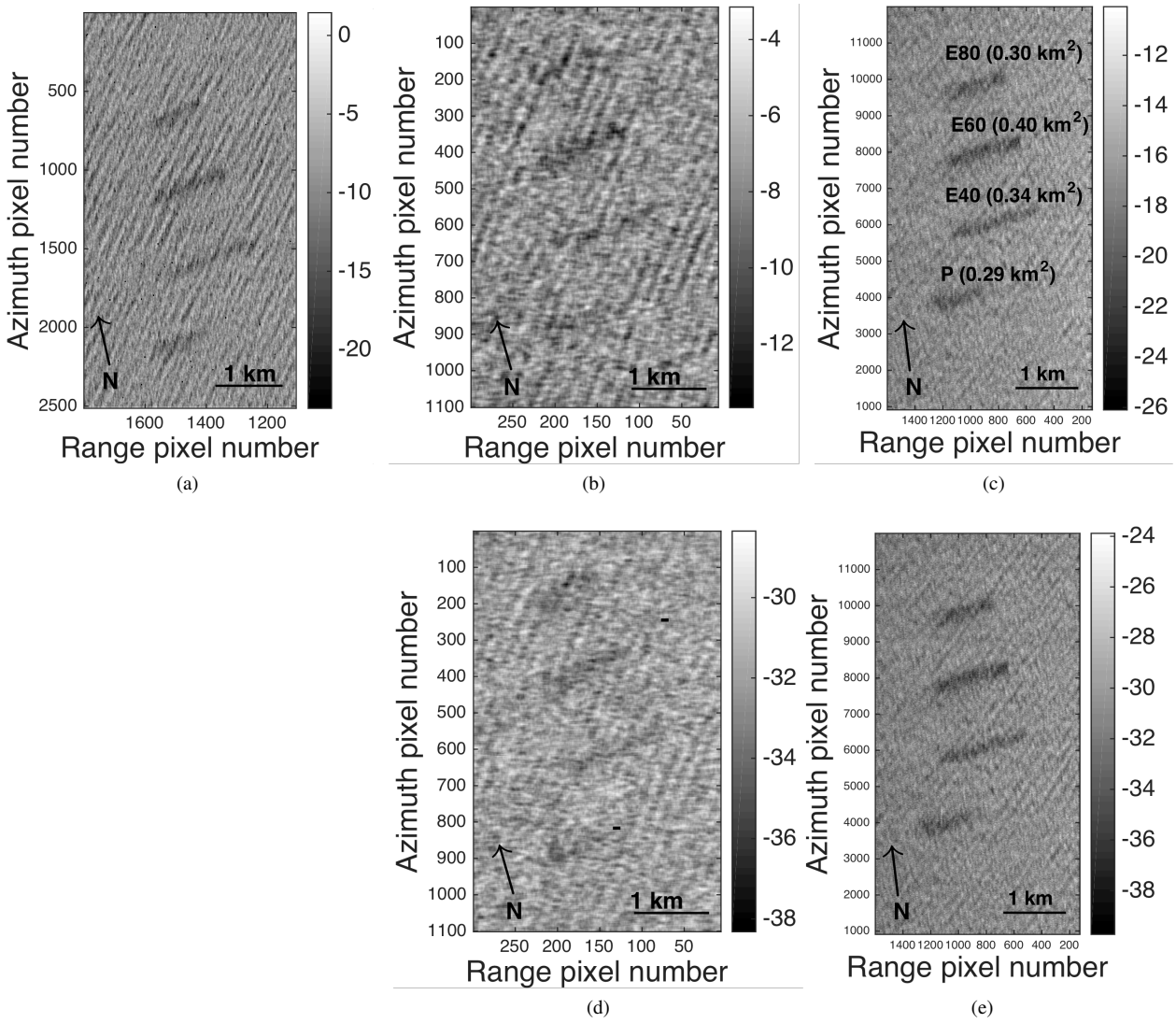

Fig. 3: Intensity images [dB] (multilooked using a 9×9 window), (a) TSX, VV, (b) RS2, VV, (c) UAVSAR, VV, (d) RS2, VH, (e) UAVSAR, VH. The slick areas given in (c) are estimated from the UAVSAR scene. TerraSAR-X ©2015 Distribution Airbus DS, Infoterra GmbH. RADARSAT-2 Data and Products ©MDA LTD. (2015) - All rights reserved. UAVSAR data are courtesy of NASA/JPL-Caltech.

Noise analyses for the three scenes here investigated are presented in Fig. 5, where the distribution of the backscatter signal within the various regions are compared to the sensor noise floors. For each ROI, the 5th, 25th, 75th and 95th percentiles are computed and plotted as horizontal lines in Fig. 5. The 50th percentiles are indicated by different symbols depending on the polarization channel. The horizontal lines are wider for VV than for HH to distinguish the two. In the case of RS2 and TSX, the distribution of the signal levels are compared to the NESZ provided with the data products. For UAVSAR, the NESZ is obtained from [28, Fig. 1(b)]. Note that no multilooking has been applied prior to the noise analysis in order to show the characteristics of the actual measured values.

It can be seen from Fig. 5 that the SNR is quite good for all three scenes. For TSX (Fig. 5(a)), which has the lowest SNR in HH and VV, the 5th percentile still lies above the noise floor for all regions, except for E60 in HH which is slightly below. All regions have the 25th percentile more than 6 dB above the NESZ, which was used as a threshold for data uncorrupted by noise in [3]. For RS2 (Fig. 5(b)), the 5th percentiles in HH and VV are all well above the NESZ. For the cross-polarization channel, the 25th percentiles lie close to the noise floor. Hence, less than 25% of the pixels in VH lies below the NESZ. In the UAVSAR (Fig. 5(c)), all channels are well above the noise floor, with all the 5th percentiles more than 6 dB above the NESZ. The HH channels lie slightly below VV in RS2 and TSX, whereas UAVSAR shows a larger difference between the two. The latter may be due to the higher incidence angle in this scene as HH decreases faster with incidence angle than VV. The UAVSAR also has a lower variability within the ROIs. Even though the noise floor is

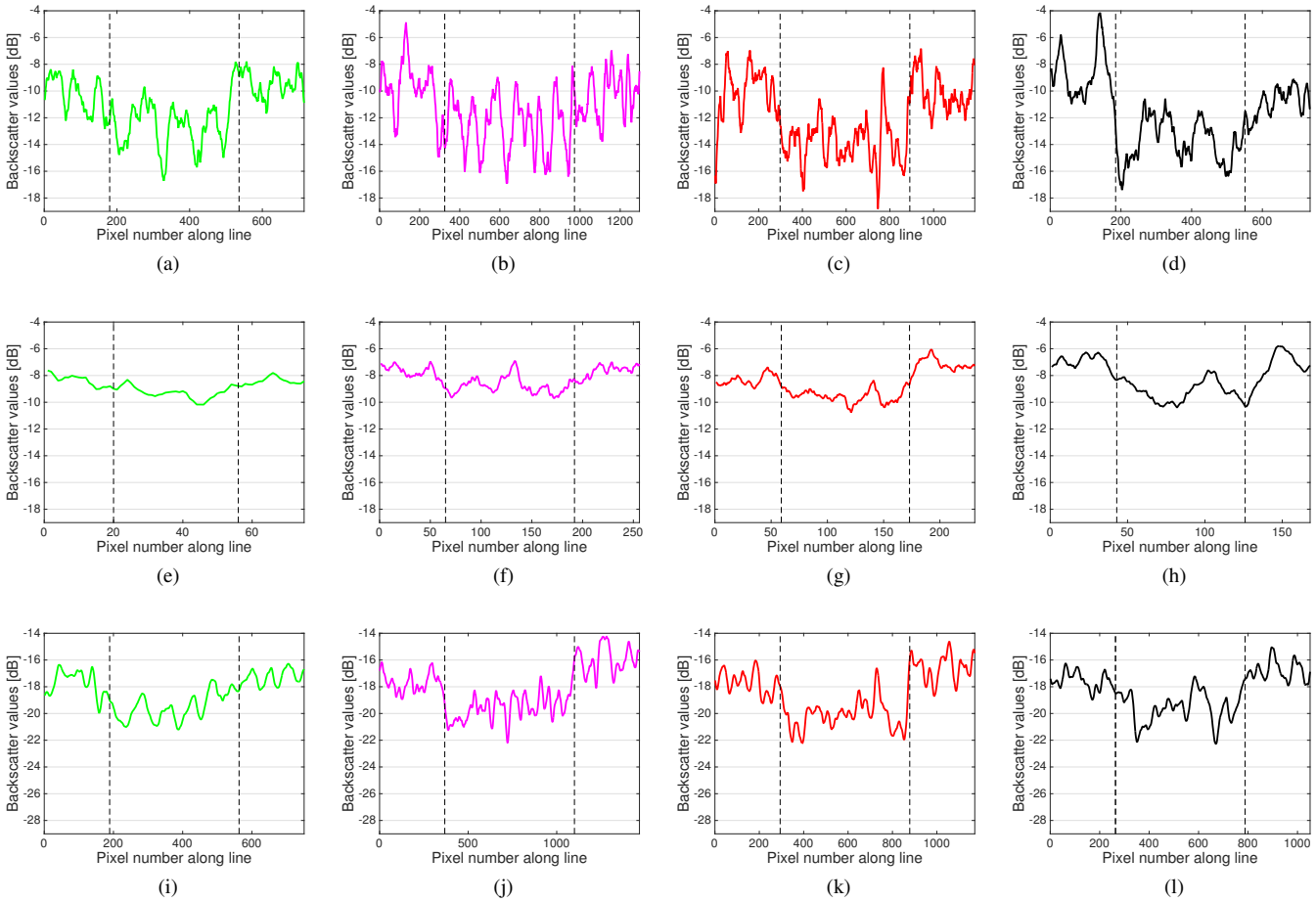

Fig. 4: Backscatter profiles along scan lines through the slicks (multilooked over 20 pixels in azimuth and along the line). Top row: TSX, middle row: RS2, bottom row: UAVSAR. Left to right: P, E40, E60 and E80. The vertical dashed lines indicate the approximate position of the edges of the slicks.

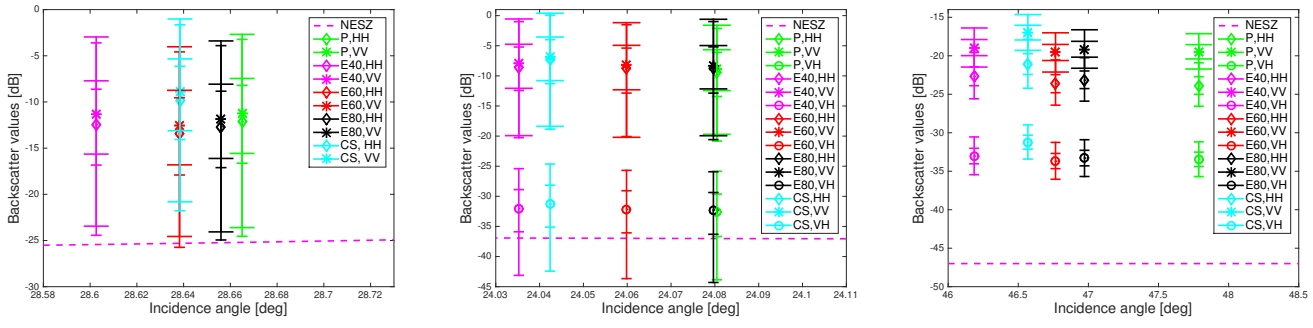

Fig. 5: Noise analyses, (a) TSX, (b) RS2, (c) UAVSAR. For each ROI, the horizontal lines indicate the 5th, 25th, 75th and 95th percentiles, and the 50th percentile is indicated by a symbol, depending on the polarization channel. The VV lines are a little wider than those for HH and VH. CS indicates clean sea.

lower in the UAVSAR, RS2 has similar, and in part higher, SNR in the co-polarization channels. In the cross-polarization channel however, the UAVSAR is superior to RS2.

The SNRs for the satellite sensors in this data set are much higher than in data from previous exercises (see [4], [10]), which is probably due to the high wind condition during NORSE2015 (see Table IV) compared to previous data collections. By comparing Fig. 5 to similar plots in [4], [10], it can be seen that the differences between regions are much lower in the current data set than in previous data collected under lower wind speeds. This agrees with other findings in the literature (see Section II-B).

Based on the noise analysis presented here, the sensor noise should have a negligible effect on the co-polarization channels for RS2 and UAVSAR. TSX are closer to the NESZ and part of the data may be somewhat affected by the proximity to the noise floor. Multipolarization characteristics are investigated in the next sections.

C. H-$\bar{\alpha}$ decomposition

The H-$\bar{\alpha}$ decomposition [35] has often been used in analysis of polarimetric SAR images to investigate the scattering mechanisms. The entropy $H \in [0, 1]$ describes the randomness of the scattering, and the mean scattering angle $\bar{\alpha} \in [0, 90]$ is used as an indicator of the type of scattering that occurs [35]. The parameters are calculated from the eigenvalues and eigenvectors of the 3×3 coherency matrix $\mathbf{T_3}$ that is defined as

$$\mathbf{T_3} = \frac{1}{L} \sum_{j=1}^{L} \mathbf{k}_j \mathbf{k}_j^{*T}, \tag{3}$$

where $\mathbf{k}_j$ is the j^{th} Pauli scattering vector $\mathbf{k} = \frac{1}{\sqrt{2}} [S_{HH} + S_{VV} \quad S_{HH} - S_{VV} \quad 2S_{VH}]^T$ (assuming reciprocity, i.e., $S_{HV} = S_{VH}$). The superscripts $*$ and T denote the complex conjugate and the vector transpose, respectively, and L is the number of samples included in the computation of the coherency matrix (here, $L = 81$). The eigenvalues λ_i and eigenvectors $\mathbf{e}_i$ ($i = 1, 2, 3$) of $\mathbf{T_3}$ are extracted and used to compute H and $\bar{\alpha}$ as

$$H = -\sum_{i=1}^{3} p_i \log_3 p_i, \tag{4}$$

and

$$\bar{\alpha} = \sum_{i=1}^{3} p_i \alpha_i, \tag{5}$$

where $p_i = \lambda_i / \sum_{i=1}^{3} \lambda_i$, and $\alpha_i = \cos^{-1}(|\mathbf{e}_i(1)|)$ is the alpha angle of the i^{th} eigenvector $\mathbf{e}_i$.

The data points can be plotted in the H-$\bar{\alpha}$ space, which is divided into nine different regions, representing different scattering types. The Bragg scattering model, which is commonly used to describe scattering from sea surfaces, occupies the region $\bar{\alpha} < 42.5°$ and $H < 0.5$ in the diagram [36].

Here, the H-$\bar{\alpha}$ decomposition is applied to the RS2 and the UAVSAR data, where the full $\mathbf{T_3}$ matrix is available. H-$\bar{\alpha}$ density plots are shown in Fig. 6 for clean sea and the E60 emulsion. It can be seen that for both sensors, both clean sea and the emulsion lie within the Bragg boundaries. Only a few data points in UAVSAR have values above $H = 0.5$. The range of the data in the H-$\bar{\alpha}$ diagram varies between the scenes, with lower values of both H and $\bar{\alpha}$ in the case of RS2. The correlation between the H and $\bar{\alpha}$ also seem to be somewhat larger in this sensor. A slight increase in H and $\bar{\alpha}$ from clean sea to the slick is observed for RS2 in Fig. 6, but all values are still well within the Bragg scattering region. Hence, no difference in scattering mechanism between slicks and sea is observed. The same is found for the other releases (not shown). This is consistent with the findings in [3], [16], where no significant contribution of a non-Bragg scatterer was found in UAVSAR data over the Deepwater Horizon oil spill. However, in [3], it was shown that instrument noise effects, which only contribute to UAVSAR at the highest incidence angles, could be misinterpreted as such. As the SNR is very good for the data investigated in the current paper, an apparent change in scattering properties due to the influence of the NESZ is not expected. Other studies have found indications of the presence of non-Bragg scattering mechanisms within oil spills, in both H and in other multipolarization parameters (see, e.g., [6]–[8], [10], [37], [38]). However, the possible presence of non-Bragg scattering mechanisms within oil slicks is not well explained, and hence a topic that still requires further investigations.

As we have quite high wind conditions in this data set, one might expect the sea surface scattering to be outside the Bragg regime, in contrast to what we observe in Fig. 6. From Table IV, it can be seen that the wind conditions were calmer on the day before the experiment, with increasing wind towards the evening. Hence, it is possible that a young wind sea was in place at the time of the SAR acquisitions. Fig. 1(b) shows that the surface has some white caps, but was not necessarily as rough as what could be expected for steadier high wind conditions. Hence, a possible reason for the low values of H and $\bar{\alpha}$ is the relatively short time the surface has been exposed to high winds. However, further investigations on H-$\bar{\alpha}$ for ocean areas in high wind conditions should be performed in the future.

D. Log-cumulant analysis

The randomness in a radar measurement is commonly attributed to two separate processes, i.e., the fully developed speckle, and the variation in the underlying radar cross section, referred to as texture. The deviation from Gaussian statistics due to the presence of texture can be evaluated by means of log-cumulants [39, translated in [40]] [41]. Log-cumulants were evaluated over surface slicks in [5], [10], and found to have a potential for differentiating mineral oil spills and simulated biogenic slicks in both RS2 and TSX.

The sample matrix log-moment (MLM) of order ν is computed from a collection of N covariance matrices as

$$\mu_\nu\{\mathbf{C}\} = \frac{1}{N} \sum_{i=1}^{N} (\ln|\mathbf{C}_i|)^\nu, \tag{6}$$

where $|\cdot|$ represents the matrix determinant. We here use the 2×2 covariance matrices computed from HH and VV given

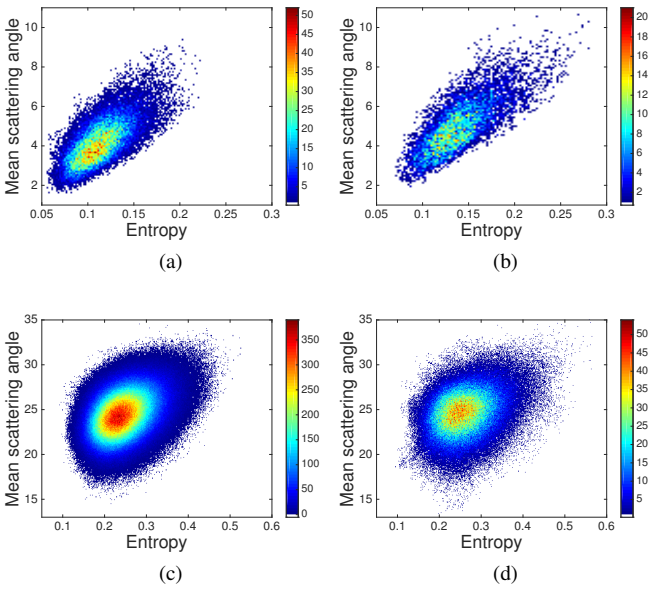

Fig. 6: Density plots of $H - \bar{\alpha}$ (computed using a 9×9 window), (a) RS2, clean sea, (b) RS2, E60, (c) UAVSAR, clean sea, (d) UAVSAR, E60. The color bar represents the number of pixels at a given location in the feature space.

as

$$\mathbf{C} = \frac{1}{L}\sum_{j=1}^{L} \mathbf{l}_j \mathbf{l}_j^{*T}, \tag{7}$$

where $\mathbf{l}_j = \frac{1}{\sqrt{2}}[S_{HH} \;\; S_{VV}]^T$ is the j^{th} lexicographic scattering vector for the dual-copolarization case. A 9×9 window is used in the computation of $\mathbf{C}$, i.e., $L = 81$.

The sample matrix log-cumulants (MLC) can be obtained from the MLMs. The first two MLCs represent the mean and variance in the log-domain, respectively, and are given by [41]

$$\kappa_1\{\mathbf{C}\} = \mu_1\{\mathbf{C}\}, \tag{8}$$

$$\kappa_2\{\mathbf{C}\} = \mu_2\{\mathbf{C}\} - \mu_1\{\mathbf{C}\}^2. \tag{9}$$

The findings in [5], [10] indicated that mineral oils had a lower κ_1 and larger κ_2 than clean sea and plant oil. It was suggested that this may be related to a higher damping and larger degree of internal variation in the mineral oil slicks, respectively (see more details in [5]).

Log-cumulants are investigated here in a similar manner as in [5]. Bootstrap sampling is used to select N covariance matrices from the manually segmented ROIs and compute the first and second order log-cumulants, i.e., $\tilde{\kappa}_1$ and $\tilde{\kappa}_2$. The $\sim$ indicates that the log-cumulants have been normalized to clean sea to account for some of the variation between scenes, e.g., due to varying incidence angle. In previous work, $N = 4000$ have been used in each computation. However, in this data set, the slicks are much smaller, and in the case of RS2, which has the lowest resolution, the number of samples must be reduced. Hence, in this study, $N = 200$ is used in each computation for RS2, whereas $N = 4000$ is used for the other two sensors. The calculation is repeated 200 times for each region for all three sensors. The results are presented in Fig. 7.

The high wind is expected to affect the log-cumulants. The low slick-sea contrasts and low variation in damping between the oil types found in Section IV-A and Section IV-B, indicate that the $\tilde{\kappa}_1$ may be more similar between the different regions than what has been found in previous low wind studies. The strong wave patterns observed in Fig. 3 are also likely to affect the statistical properties of both slicks and clean sea. It may contribute to the internal variation described by κ_2, and can possibly overpower the potential differences between regions, reducing the differences in κ_2. It will also alter the backscatter level of slicks and sea, reducing the usefulness of κ_1 for region separation.

These expectations correspond well with what we observe in Fig. 7, which does not show similar differences between the slicks and sea and between the plant oil and mineral oils as previously observed, for any of the three sensors. The RS2 results may be directly compared to those in [5] (with wind speeds < 5 m/s), and it can be seen that the current $\tilde{\kappa}_1$ and $\tilde{\kappa}_2$ values for the emulsions are much lower than in the previous cases. Hence, the separability between classes in the log-cumulant diagram is reduced under high winds. We note that these slicks had not been on the surface long and the E80 slick in particular was not fully developed.

Fig. 7 also shows some between-sensor variation. RS2 has the lowest $\tilde{\kappa}_1$, reflecting the poorer contrast discussed in Section IV-A. In both UAVSAR and RS2, most slicks have $\tilde{\kappa}_2$ values around zero, i.e., little difference in the internal region variations between slicks and clean sea, whereas TSX has larger values. Similar findings were observed in [10], where three pairs of near coincident RS2 and TSX scenes were investigated in terms of unnormalized log-cumulants and a higher texture was observed in TSX compared to in RS2 data. Possible explanations in [10] included the higher resolution of TSX, the difference in frequency (difference in relative roughness) and a difference in scattering properties, possibly related to smaller incidence angles in TSX. If we look at the unnormalized values in the current data set (not shown here), we find an increase in κ_2 within all regions from RS2 to UAVSAR to TSX. In the current data set, the RS2 and the TSX scenes have more similar incidence angles ($\sim 24^\circ$ and $\sim 28.6^\circ$, respectively), hence the observation geometry should be less of a factor. The fact that the UAVSAR data show higher values of κ_2 than RS2 indicates that it may be the resolution rather than the frequency that causes the difference in log-cumulants. In range direction, which is the direction of largest slick extent, the resolution is highest in TSX and lowest in RS2, which may hence cause the observed between-sensor variation in the κ_2 values. As the surface resolution cells are smaller for TSX and UAVSAR, they will contain a lower number of wave trains, which can give more inhomogeneous regions and partially developed speckle, leading to increased texture (see [10]).

E. Other multipolarization parameters

A variety of multipolarization parameters have been investigated in the literature for the purpose of oil spill detection

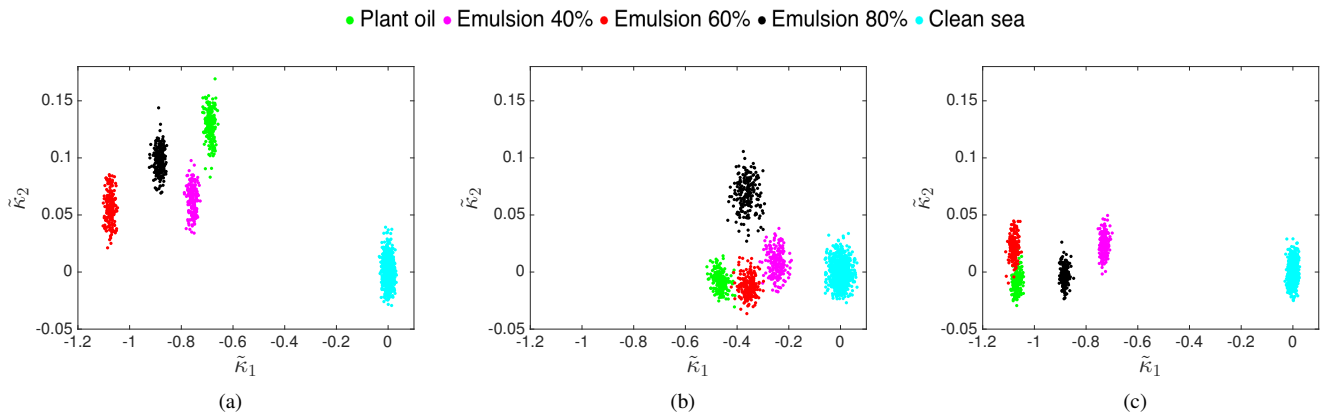

Fig. 7: Log-cumulant diagrams, (a) TSX, (b) RS2, (c) UAVSAR. Each point is calculated from 4000 samples for TSX and UAVSAR, and 200 samples for RS2.

and characterization. In [4], a set of eight multi-polarization features was investigated and compared for the purpose of discriminating mineral oils from simulated biogenic slicks (plant oil). The features were computed based on HH and VV only, due to the low cross-polarization SNR as discussed in section IV-B. In the current study, we evaluate the eight features applied in [4], in addition to several other multipolarization descriptors that have been proposed for oil spill observation, all computed from HH and VV only, using a 9×9 sliding window. The features and their definitions are listed in Table VI. The parameters H', α'_1 and λ'_1 are the dual-copolarization versions of the parameters defined in Section IV-C. These are extracted from the 2×2 submatrix of the $\mathbf{T_3}$ defined in (3) obtained by excluding the cross-polarization element in $\mathbf{k}$. The subscript $'$ is used to separate this version from the quad-polarization version. Ensemble averaging is indicated by $\langle \cdot \rangle$ and $\Re$ denotes the real part.

In order to quantitatively evaluate the features' abilities to detect and characterize the slicks in these scenes, a separability measure is applied. The Fischer's discriminant ratio (FDR) is defined as [42]

$$\mathrm{FDR} = \frac{(m_k - m_l)^2}{\sigma_k^2 + \sigma_l^2} \tag{10}$$

where m_k and σ_k^2 are the mean and variance of the feature values within region k, respectively. The FDR can take values from 0 and upwards, and can be used to quantify the separability capabilities of individual features [42]. Table VI presents the FDR between each slick and clean sea for the multi-polarization features considered. The VV intensity is included for comparison.

1) Slick-sea separability: It can be seen from Table VI that the maximum slick-sea separabilities vary between scenes and regions, but are mainly found in the same five parameters, i.e., VV intensity, μ, $span$, λ'_1 and r_{CO} (values given in bold). For most regions in RS2 and UAVSAR, VV intensity has the best separability, whereas μ has the highest FDR in all cases for TSX. The separability between slicks and clean sea is largest for P and E60 in UAVSAR and RS2, and for E60 and E80 in TSX.

The particular sensor that provides the largest separability varies with feature. For the five features with the best slick-sea separability (i.e., VV intensity, μ, $span$, λ'_1 and r_{CO}) (see Table VI for definition), the highest FDRs are generally found in UAVSAR. As these parameters are mainly connected to the backscatter level, this corresponds well with what is observed in the intensity images in Fig. 3. For the other features, the highest separability is often found in RS2 with the second highest values in TSX. The fact that RS2 produces higher FDR than TSX may be surprising when comparing the two scenes in Fig. 3, where TSX has a better visual slick-sea contrast. The within-region variations are large in the case of TSX, as can be observed in both Fig. 4 and Fig. 5, decreasing the FDR even though the contrast may be better than in RS2. In addition, the slick segmentations in RS2 are more unreliable, as discussed in Section IV-A. Hence, it is possible that only a part of the slicks is segmented out due to the poor contrast. Because of this, we consider the RS2 results to be less reliable, and the overall performance of TSX to be superior to that of RS2.

2) Separability between slick types: Although the VV intensity performs better than most multipolarization features when it comes to slick-sea separability under these conditions, several multipolarization features show higher FDR than the intensity when it comes to between-slicks separabilities (not shown here). Hence, multipolarization parameters perform better when it comes to characterization. However, the separabilities between slick regions are generally lower than that between slicks and clean sea, often by at least one order of magnitude. Which slicks are separated the best varies among the features and sensors. The separability is generally largest for P-E40 and E40-E60 in UAVSAR, for P-E40 and P-E80 in RS2, and for P-E60 and E40-E60 in TSX. The separability between the two emulsions with largest oil content is low for all three sensors for the scenes used in this analysis. This could be at least in part due to the E80 slick being less developed, as it was released last. The features that stand out when it comes to between-slick separability are γ_{CO} and μ for UAVSAR, $span$, μ and r_{CO} for RS2 and μ, $span$, γ_{CO} and λ'_1 for TSX. It is noted that the two features identified as the most promising in [4], i.e., μ and r_{CO}, also here produce the best visual slick-sea contrast of the eight features from [4], and perform well when quantified using the FDR.

TABLE VI: Overview of the investigated multipolarization features (computed using a 9×9 window) and their slick-sea separability. The Fischer's discriminant ratio (FDR) is given for P-sea / E40-sea / E60-sea / E80-sea. Higher values of FDR indicates better separability between regions. The FDR for the five features which give the overall highest slick-sea separabilities are given in bold. The references included are examples of studies where the features have previously been applied for oil spill observation. References in parentheses indicate that the corresponding quad-polarization version of the feature (including the cross-polarization channel) is applied.

Feature	TSX	RS2	UAVSAR
Entropy [4] ([3], [6], [37], [38], [43]–[47]) $H' = -\sum_{i=1}^{2} p_i \log_2 p_i$	0.14 / 0.21 / 0.40 / 0.29	0.89 / 0.31 / 0.50 / 0.35	0.07 / 0.07 / 0.05 / 0.05
Alpha angle of largest eigenvalue [4] $\alpha_1' = \cos^{-1}(\lvert\mathbf{e_1}(1)\rvert)$	0.01 / 0.05 / 0.04 / 0.02	0.11 / 0.00 / 0.02 / 0.01	0.01 / 0.03 / 0.01 / 0.02
Anisotropy [4] ([3], [37], [43], [48]) $A' = \frac{\lambda_1' - \lambda_2'}{\lambda_1' + \lambda_2'}$	0.14 / 0.19 / 0.34 / 0.26	0.86 / 0.31 / 0.48 / 0.35	0.06 / 0.07 / 0.05 / 0.05
Largest eigenvalue λ_1' ([3])	**0.23 / 0.31 / 0.61 / 0.45**	**1.2 / 0.35 / 0.77 / 0.41**	**1.2 / 0.60 / 1.1 / 0.83**
Geometric intensity [4], [10] $\mu = (\det(\mathbf{T}))^{1/2}$	**0.35 / 0.45 / 0.89 / 0.59**	**1.1 / 0.28 / 0.64 / 0.43**	**1.2 / 0.57 / 1.2 / 0.85**
Copolarization power ratio [3], [4], [10] $\gamma_{CO} = \frac{\langle \lvert S_{HH}\rvert^2 \rangle}{\langle \lvert S_{VV}\rvert^2 \rangle}$	0.01 / 0.01 / 0.00 / 0.01	0.06 / 0.01 / 0.00 / 0.00	0.04 / 0.04 / 0.00 / 0.00
Std. of copolarized phase difference [4], [6], [8], [49], [50] $\sigma_{\phi CO} = \sqrt{\langle(\phi_{HH} - \phi_{VV})^2\rangle - (\langle\phi_{HH} - \phi_{VV}\rangle)^2}$	0.17 / 0.17 / 0.39 / 0.26	0.20 / 0.17 / 0.16 / 0.15	0.05 / 0.02 / 0.02 / 0.02
Magnitude of the copol. correlation coefficient [4], [47], [50] $\rho_{CO} = \left\lvert \frac{\langle S_{HH} S_{VV}^* \rangle}{\sqrt{\langle \lvert S_{HH}\rvert^2 \rangle \langle \lvert S_{VV}\rvert^2 \rangle}} \right\rvert$	0.14 / 0.19 / 0.34 / 0.26	0.87 / 0.31 / 0.48 / 0.34	0.10 / 0.04 / 0.04 / 0.04
Real part of the copol. cross product [4], [6], [7], [10], [27], [44] $r_{CO} = \left\lvert \Re\left(\left\langle S_{HH} S_{VV}^* \right\rangle\right) \right\rvert$	**0.23 / 0.30 / 0.60 / 0.44**	**1.3 / 0.35 / 0.77 / 0.41**	**1.1 / 0.49 / 0.96 / 0.70**
$Span$ ([47]) $Span = \left\langle \lvert S_{HH}\rvert^2 \right\rangle + \left\langle \lvert S_{VV}\rvert^2 \right\rangle$	**0.24 / 0.31 / 0.62 / 0.45**	**1.3 / 0.35 / 0.78 / 0.41**	**1.2 / 0.61 / 1.1 / 0.85**
Polarization difference [10], [51] $PD = \left\langle \lvert S_{VV}\rvert^2 \right\rangle - \left\langle \lvert S_{HH}\rvert^2 \right\rangle$	0.15 / 0.11 / 0.28 / 0.23	0.01 / 0.08 / 0.10 / 0.11	0.91 / 0.71 / 1.0 / 0.75
VV intensity $\left\langle \lvert S_{VV}\rvert^2 \right\rangle$	**0.26 / 0.33 / 0.67 / 0.49**	**1.2 / 0.38 / 0.80 / 0.44**	**1.3 / 0.73 / 1.3 / 0.92**

3) Comparison to low wind results: Due to space limitations, plots of all multipolarization features listed in Table VI for all scenes are not shown here. As a representative example of the features' appearances and distributions, the μ images and histograms are included in Fig. 8. This feature is chosen as it is one of the features that perform best in terms of FDR and that has also previously been found useful for slick characterization [4]. The histograms in Fig. 8 show that there is some degree of separation between clean sea and slicks, whereas the different slick types are overlapping in all sensors. This differs from the findings in [4], [10], where much better separations between slicks and clean sea and between mineral oils and plant oils were observed. None of the features included in Table VI is found to show any clear differences between the various slick types for the scenes investigated here.

As discussed in the preceding sections, the high wind conditions can cause a decrease in the slick-sea contrast, and a loss of potential differences in the damping characteristics between slick types. This may be reflected in the low separability of the multipolarization features between the different regions in the scenes. In addition, differences in multipolarization parameters between mineral oils and clean sea/look-alikes are often attributed to a change in scattering mechanism from Bragg to non-Bragg scattering. In Section IV-C, H-$\bar{\alpha}$ plots indicated a dominance of Bragg scatter for both clean sea and slicks for RS2 and UAVSAR. Hence, multipolarization features related to a change in scattering properties may not perform well for region separation in this case. It has been shown that low SNR can produce multipolarization feature values that could be misinterpreted as a change in scattering type [3]. In the data set here investigated, the SNR is high and the noise should have a negligible effect on the results. Hence, the large SNR may in fact also cause less between-region variations in multipolarization parameters than for data with poorer SNRs. Although poor SNR could benefit slick detection, it precludes slick characterization. Conclusions on whether the reduced between-region discrimination here observed is due to slick properties, high SNR, other effects related to high wind, or a combination of these and/or other factors, requires further data collections and analysis.

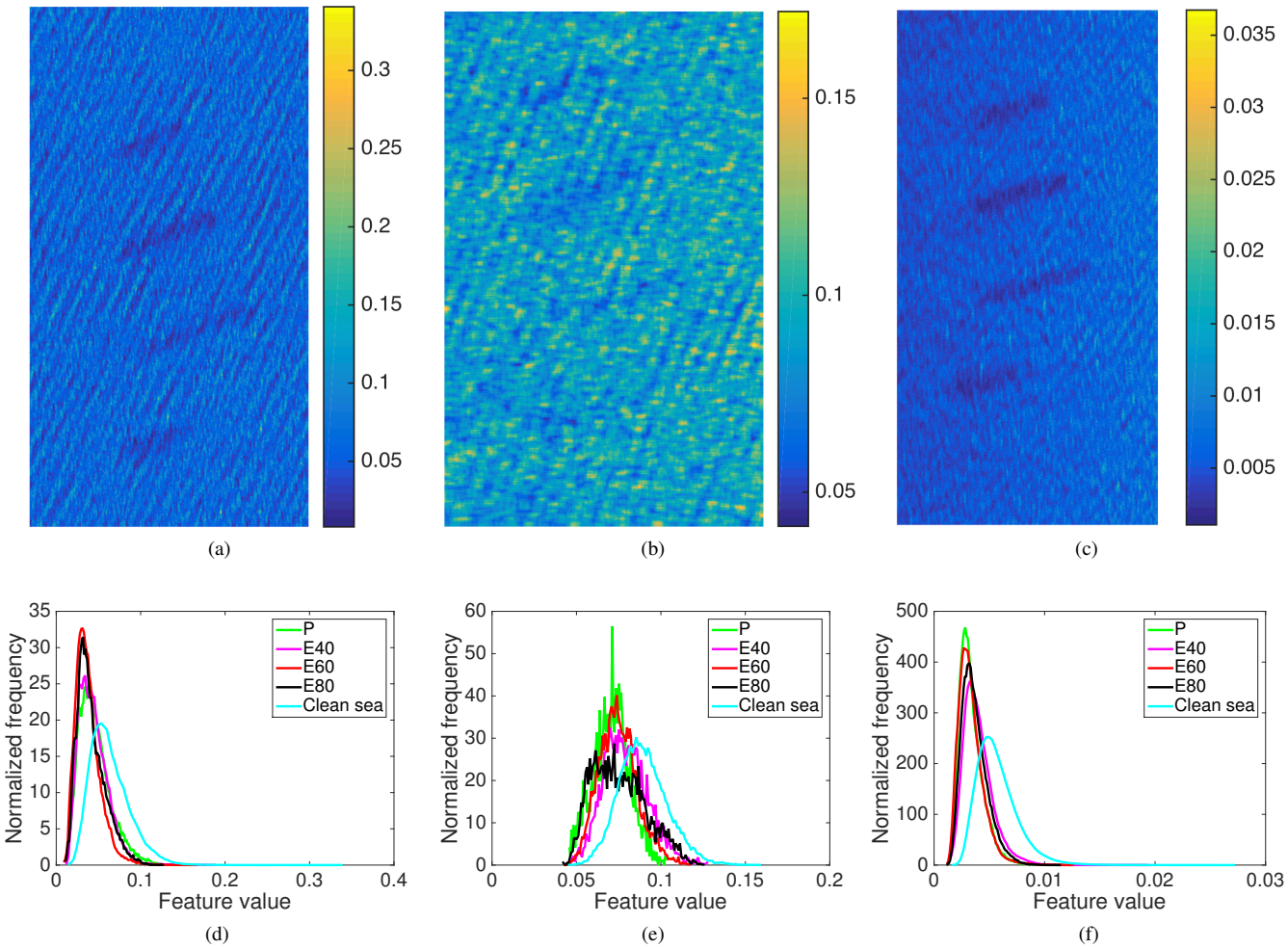

Fig. 8: μ images and histograms of feature values within the ROIs (computed using a 9×9 window), (a) and (d) TSX, (b) and (e) RS2, (c) and (f) UAVSAR.

V. Conclusions

A comparison of near-coincident multipolarization data from RS2, TSX and UAVSAR has been presented. All three sensors are able to detect the four slicks of varying properties, even though the slicks are small (0.2 m^3 for the plant oil release and 0.5 m^3 for the emulsions) and the wind speed of $\sim$12 m/s is in the upper part of the range where oil spill detection is considered possible. The detectability is better in TSX and UAVSAR than in RS2, with the highest slick-sea contrasts in UAVSAR. This may be due to a combination of sensor-related parameters, including high incidence angles, high SNR and fine resolution. The signal damping within slicks is lower than observed in previous studies, as are the differences in the damping among slick types. This is expected under high wind conditions, e.g., due to reduced contrast in surface roughness.

The high wind results in much better SNR than observed in the preceding studies, and even the RS2 cross-polarization channels have more than 75% of the data above the NESZ. Both RS2 and UAVSAR have very high SNRs in the copolarization channels, whereas TSX produces the lowest SNRs. The UAVSAR is superior to RS2 when it comes to cross-polarization SNR.

Multipolarization parameters that have previously been applied for discrimination between slick types are not found useful for that purpose in the instance here studied. This may be due to effects of the high wind (e.g., wave pattern affecting the backscatter characteristics, reduced roughness contrasts, reduced damping, and high SNR), possibly in combination with the small sizes of the slicks. A need for further studies on the effect of the SNR on the multipolarization feature values and interpretation of these are emphasized. H-$\bar{\alpha}$ analysis of RS2 and UAVSAR data shows that all regions are within the Bragg regime for both sensors, despite the high wind conditions. The images used in this analysis are a snapshot of the slick conditions between 1 and 1.7 hours following the releases. Further investigation of the time series of UAVSAR images is ongoing to determine whether higher contrast between the slicks occurred at other times during the slick evolution.

The UAVSAR sensor gives the overall best results in terms of slick detectability and SNR, whereas TSX is the preferred satellite sensor under the given conditions. Further comparisons of the sensors characterization capabilities should

be performed under lower winds, as the current wind speed may be too high for this task, using existing multipolarization descriptors. However, further research focusing on oil vs. look-alike discrimination under high wind conditions is also required.

ACKNOWLEDGEMENT

The authors would like to thank NOFO for including our experiment in their exercise and for providing ground truth data. Thanks to scientists at the Norwegian Meteorological Institute for collecting metocean data, and to KSAT for providing detection reports. Thanks also to Harald Johnsen at the Northern Research Institute for retrieval of SAR wind and wave information, and to Anthony Doulgeris and Martine M. Espeseth at UiT for useful discussions. The research described in this paper was carried out in part at the Jet Propulsion Laboratory, California Institute of Technology, under a contract with the National Aeronautics and Space Administration. UAVSAR data are courtesy of NASA/JPL-Caltech. Radarsat-2 data is provided by NSC/KSAT under the Norwegian-Canadian Radarsat agreement 2015. TerraSAR-X ©2015 Distribution Airbus DS, Infoterra GmbH.

REFERENCES

[1] W. Alpers and H. A. Espedal, "Oils and surfactants," in *Synthetic Aperture Radar Marine User's Manual*, C. R. Jackson and J. R. Apel, Eds. U.S. Department of Commerce, National Oceanic and Atmospheric Administration, Sep. 2004, pp. 263–275.

[2] M. K. McNutt, R. Camilli, T. J. Crone, G. D. Guthrie, P. A. Hsieh, T. B. Ryerson, O. Savas, and F. Shaffer, "Review of flow rate estimates of the Deepwater Horizon oil spill," *Proc. National Academy of Sciences*, vol. 109, no. 50, pp. 20 260–20 267, Dec. 2012.

[3] B. Minchew, C. E. Jones, and B. Holt, "Polarimetric analysis of backscatter from the Deepwater Horizon oil spill using L-band synthetic aperture radar," *IEEE Trans. Geosci. Remote Sens.*, vol. 50, no. 10, pp. 3812–3830, Oct. 2012.

[4] S. Skrunes, C. Brekke, and T. Eltoft, "Characterization of marine surface slicks by Radarsat-2 multipolarization features," *IEEE Trans. Geosci. Remote Sens.*, vol. 52, no. 9, pp. 5302–5319, Sept. 2014.

[5] S. Skrunes, C. Brekke, and A. P. Doulgeris, "Characterization of low backscatter ocean features in dual-copolarization SAR using log-cumulants," *IEEE Geosci. Remote Sens. Lett.*, vol. 12, no. 4, pp. 836–840, Apr. 2015.

[6] M. Migliaccio, F. Nunziata, and A. Buono, "SAR polarimetry for sea oil slick observation," *Int. J. Remote Sens.*, vol. 32, no. 12, pp. 3243–3273, 2015.

[7] F. Nunziata, A. Gambardella, and M. Migliaccio, "On the Mueller scattering matrix for SAR sea oil slick observation," *IEEE Geosci. Remote Sens. Lett.*, vol. 5, no. 4, pp. 691–695, Oct. 2008.

[8] M. Migliaccio, F. Nunziata, and A. Gambardella, "On the co-polarized phase difference for oil spill observation," *Int. J. Remote Sens.*, vol. 30, no. 6, pp. 1587–1602, Mar. 2009.

[9] M. Gade, W. Alpers, H. Hühnerfuss, H. Masuko, and T. Kobayashi, "Imaging of biogenic and anthropogenic ocean surface films by the multifrequency/multipolarization SIR-C/X-SAR," *J. Geophys. Res.*, vol. 103, no. C9, pp. 18,851–18,866, Aug. 1998.

[10] S. Skrunes, C. Brekke, T. Eltoft, and V. Kudryavtsev, "Comparing near coincident C- and X-band SAR acquisitions of marine oil spills," *IEEE Trans. Geosci. Remote Sens.*, vol. 53, no. 4, pp. 1958–1975, Apr. 2015.

[11] W. Alpers and H. Hühnerfuss, "Radar signatures of oil films floating on the sea surface and the marangoni effect," *J. Geophys. Res.*, vol. 93, no. C4, pp. 3642–3648, Apr. 1988.

[12] B. Minchew, "Determining the mixing of oil and sea water using polarimetric synthetic aperture radar," *Geophys. Res. Lett.*, vol. 39, 2012.

[13] G. R. Valenzuela, "Theories for the interaction of electromagnetic and oceanic waves - a review," *Boundary-Layer Meteorology*, vol. 13, no. 1-4, pp. 61–85, Jan. 1978.

[14] F. Girard-Ardhuin, G. Mercier, F. Collard, and R. Garello, "Operational oil-slick characterization by SAR imagery and synergistic data," *IEEE J. of Oceanic Eng.*, vol. 30, no. 3, pp. 487–495, Jul. 2005.

[15] N. Pinel, C. Bourlier, and I. Sergievskaya, "Two-dimensional radar backscattering modeling of oil slicks at sea based on the model of local balance: Validation of two asymptotic techniques for thick films," *IEEE Trans. Geosci. Remote Sens.*, vol. 52, no. 5, pp. 2326–2338, May 2014.

[16] D. Latini, F. D. Frate, and C. E. Jones, "Multi-frequency and polarimetric quantitative analysis of the Gulf of Mexico oil spill event comparing different SAR systems," *Remote Sens. Environ.*, (in review), 2015.

[17] F. Ulaby, R. K. Moore, and A. K. Fung, *Microwave remote sensing, active and passive, volume II; Radar remote sensing and emission theory*. Artech House Inc., Norwood, USA, 1986.

[18] D.-J. Kim, W. Moon, and Y.-S. Kim, "Application of TerraSAR-X data for emergent oil-spill monitoring," *IEEE Trans. Geosci. Remote Sens.*, vol. 48, no. 2, pp. 852 –863, Feb. 2010.

[19] V. Wismann, M. Gade, W. Alpers, and H. Hühnerfuss, "Radar signatures of marine mineral oil spills measured by an airborne multi-frequency radar," *Int. J. Remote Sens.*, vol. 19, no. 18, pp. 3607–3623, 1998.

[20] F. D. Frate, A. Giacomini, D. Latini, D. Solimini, and W. J. Emery, "The Gulf of Mexico oil rig accident: analysis by different SAR satellite images," in *Proc. of SPIE*, vol. 8179, Oct., 2011.

[21] S. K. Sasamal and M. V. Rao, "Oil spill experiment using airborne DLR ESAR off the coast of Diu, India," *Marine Pollution Bulletin*, vol. 94, pp. 228–234, 2015.

[22] F. M. Monaldo and R. Beal, "Wind speed and direction," in *Synthetic Aperture Radar Marine User's Manual*, C. Jackson and J. Apel, Eds. U.S. Department of Commerce, National Oceanic and Atmospheric Administration, Washington DC, USA, Sep. 2004, pp. 305–320.

[23] P. W. Vachon, F. M. Monaldo, B. Holt, and S. Lehner, "Ocean surface waves and spectra," in *Synthetic Aperture Radar Marine User's Manual*, C. Jackson and J. Apel, Eds. U.S. Department of Commerce, National Oceanic and Atmospheric Administration, Washington DC, USA, Sep. 2004, pp. 139–169.

[24] A. H. S. Solberg, "Remote sensing of ocean oil-spill pollution," *Proc. IEEE*, vol. 100, no. 10, pp. 2931–2945, Oct. 2012.

[25] M. Fingas and C. Brown, "Review of oil spill remote sensing," *Marine Pollution Bulletin*, vol. 83, pp. 9–23, 2014.

[26] Y. Chan-Su, P. Seong-Min, O. Yisok, and O. Kazuo, "An analysis of the radar backscatter from oil-covered sea surfaces using moment method and Monte-Carlo simulation: preliminary results," *Acta Oceanologica Sinica*, vol. 32, no. 1, pp. 59–67, 2013.

[27] C. Brekke, C. Jones, S. Skrunes, B. Holt, M. Espeseth, and T. Eltoft, "Cross-correlation between polarization channels in SAR imagery over oceanographic features," *IEEE Geosci. Remote Sens. Lett.*, 2016 (accepted).

[28] A. G. Fore, B. D. Chapman, B. P. Hawkins, S. Hensley, C. E. Jones, T. R. Michel, and R. J. Muellerschoen, "UAVSAR polarimetric calibration," *IEEE Trans. Geosci. Remote Sens.*, vol. 53, no. 6, pp. 3481–3491, Jun. 2015.

[29] German Aerospace Center, "TerraSAR-X ground segment basic product specification document," URL: http://www.dlr.de/dlr/Portaldata/1/Resources/documents/TX-GS-DD-3302_Basic-Product-Specification-Document_1_7.pdf, Visited 30. Jun. 2014, Oct. 2010.

[30] MacDonald, Dettwiler and Associates Ltd., "Radarsat-2 product description," Tech. Rep., 2014.

[31] MetOcean, URL:http://www.metocean.com/products/metocean-systems/current-monitoring/isphere.

[32] ——, URL: http://www.metocean.com/products/defence-security/search-rescue/isldmbtm.

[33] H. Johnsen and F. Collard, "SAR wave mode processing - improvements towards SENTINEL-1 mission," in *Proc. SeaSAR*, vol. 709, Tromsø, Norway, Jun. 2012, pp. 85–89.

[34] ——, "Sentinel-1 ocean swell wave spectra (OSW) algorithm definition," Norut, URL:https://earth.esa.int/web/sentinel/user-guides/sentinel-1-sar/document-library/-/asset_publisher/1dO7RF5fJMbd/content/sentinel-1-ocean-swell-wave-spectra-osw-algorithm-definition, 2011.

[35] S. R. Cloude and E. Pottier, "An entropy based classification scheme for land applications of polarimetric SAR," *IEEE Trans. Geosci. Remote Sens.*, vol. 35, no. 1, pp. 68 –78, Jan. 1997.

[36] J.-S. Lee and E. Pottier, *Polarimetric Radar Imaging, from basics to applications*. CRC Press, Taylor and Francis Group, Boca Raton, USA, 2009.

[37] M. Migliaccio, A. Gambardella, and M. Tranfaglia, "SAR polarimetry to observe oil spills," *IEEE Trans. Geosci. Remote Sens.*, vol. 45, no. 2, pp. 506 –511, Feb. 2007.
[38] W. Tian, Y. Shao, J. Yuan, S. Wang, and Y. Liu, "An experiment for oil spill recognition using RADARSAT-2 image," in *Proc. IEEE Int. Geosci. Remote Sens. Symp.*, Honolulu, USA, Jul. 2010, pp. 2761 –2764.
[39] J.-M. Nicolas, "Introduction aux statistiques de deuxième espèce: applications des logs-moments et des logs-cumulants à l'analyse des lois d'images radar," *Traitement du Signal*, vol. 19, no. 3, pp. 139–167, 2002.
[40] J.-M. Nicolas and S. N. Anfinsen, "Introduction to second kind statistics: Application of log-moments and log-cumulants to the analysis of radar image distributions," Technical note, translation from French of [39]. URL: http://eo.uit.no/publications/JMN-TRANS-12.pdf, Visited 30. Jun. 2014, May 2012.
[41] S. N. Anfinsen and T. Eltoft, "Application of the matrix-variate Mellin transform to analysis of polarimetric radar images," *IEEE Trans. Geosci. Remote Sens.*, vol. 49, no. 6, pp. 2281–2295, Jun. 2011.
[42] S. Theodoridis and K. Koutroumbas, *Pattern Recognition*, 3rd ed. Academic Press, San Diego, CA, USA, 2006.
[43] D. L. Schuler and J.-S. Lee, "Mapping ocean surface features using biogenic slick-fields and SAR polarimetric decomposition techniques," in *IEE Proc. Radar, Sonar Navig.*, vol. 153, no. 3, Jun. 2006, pp. 260 – 270.
[44] M. Migliaccio, A. Gambardella, F. Nunziata, M. Shimada, and O. Isoguchi, "The PALSAR polarimetric mode for sea oil slick observation," *IEEE Trans. Geosci. Remote Sens.*, vol. 47, no. 12, pp. 4032 –4041, Dec. 2009.
[45] M. Migliaccio, F. Nunziata, A. Montuori, and C. E. Brown, "Marine added-value products using RADARSAT-2 fine quad-polarization," *Can. J. Remote Sens.*, vol. 37, no. 5, pp. 443–451, 2011.
[46] B. Zhang, W. Perrie, X. Li, and W. G. Pichel, "Mapping sea surface oil slicks using RADARSAT-2 quad-polarization SAR image," *Geophys. Res. Lett.*, vol. 38, no. 10, May 2011.
[47] W. Wenguang, L. Fei, W. Peng, and W. Jun, "Oil spill detection from polarimetric SAR image," in *Proc. IEEE Int. Conf. Signal Process.*, Oct. 2010, pp. 832 –835.
[48] J. Fortuny-Guasch, "Improved oil slick detection and classification with polarimetric SAR," in *Proc. Workshop POLinSAR*, Frascati, Italy, Jan. 2003.
[49] M. Migliaccio, F. Nunziata, A. Montuori, X. Li, and W. G. Pichel, "A multifrequency polarimetric SAR processing chain to observe oil fields in the Gulf of Mexico," *IEEE Trans. Geosci. Remote Sens.*, vol. 49, no. 12, pp. 4729–4737, Dec. 2011.
[50] D. Velotto, M. Migliaccio, F. Nunziata, and S. Lehner, "Dual-polarized TerraSAR-X data for oil-spill observation," *IEEE Trans. Geosci. Remote Sens.*, vol. 49, no. 12, pp. 4751–4762, Dec. 2011.
[51] V. Kudryavtsev, B. Chapron, A. Myasoedov, F. Collard, and J. Johannessen, "On dual co-polarized SAR measurements of the ocean surface," *IEEE Geosci. Remote Sens. Lett.*, vol. 10, no. 4, pp. 761–765, 2013.

Stine Skrunes (S'12-M'15) received the M.Sc. and Ph.D. degrees from the Department of Physics and Technology, UiT The Arctic University of Norway, Tromsø, Norway, in 2011 and 2014, respectively. She is currently a Postdoc at the same department, with the Centre for Integrated Remote Sensing and Forecasting for Arctic Operations (CIRFA). Her current research interests include remote sensing of ocean areas, specifically by polarimetric SAR and with a focus on marine oil pollution.

Camilla Brekke (M'12) received the Cand.Sci. and Ph.D. degrees from the University of Oslo, Oslo, Norway, in 2001 and 2008, respectively. In 2001, she was a System Developer with Ericsson, Asker, Norway. From 2001 to 2002, she was a Young Graduate Trainee with the European Space Agency, Noordwijk, The Netherlands. From 2002 to 2009, she was a Scientist with the Norwegian Defense Research Establishment (FFI), Kjeller, Norway. In 2009, she joined the Department of Physics and Technology, UiT The Arctic University of Norway (UiT), Tromsø, Norway, as an Associate Professor. From October 2012 to January 2013, she was a Visiting Scientist with the Jet Propulsion Laboratory, Pasadena, CA, USA. At UiT she is currently with the Earth Observation Laboratory and Centre for Integrated Remote Sensing and Forecasting for Arctic Operations. Her current research interests cover signal and image processing of synthetic aperture radar data for arctic and marine applications.

Cathleen E. Jones is a radar scientist at NASA's Jet Propulsion Laboratory, California Institute of Technology, where her main research is focused on using radar remote sensing for studying natural disasters and monitoring critical infrastructure, primarily using high resolution L-band PolSAR and InSAR based on UAVSAR data. Her research includes development of methods for determining oil slick characteristics and identifying levee deformation, seepage, and general subsidence rates using SAR. In addition she has done work detecting sinkhole presursors in InSAR-challenged areas. She received a B.S. in physics from Texas A&M and a Ph.D. in physics from the California Institute of Technology.

Benjamin Holt is a research scientist in the Ocean Circulation group within the Earth Science Section at the Jet Propulsion Laboratory, California Institute of Technology, which he joined in 1978. He received the B.S. from Stanford University in 1972 and the M.S. in physical oceanography from the University of Southern California in 1988. His research interests include using multi-sensor remote sensing data to examine the geophysical state of polar sea ice and snow, coastal oceanography and circulation, and the detection of marine pollutants. In addition, he is also involved with new instrument development and techniques for microwave measurement of sea ice thickness.